

Ultra-Broadband Entangled Photons on a Nanophotonic Chip

CNF Project Number: 1997-11

Principal Investigator(s): Qiang Lin^{1,2}

User(s): Usman A. Javid¹, Jingwei Ling², Mingxiao Li², Yang He²

Affiliation(s): 1. Institute of Optics, University of Rochester, Rochester NY;

2. Department of Electrical and Computer Engineering, University of Rochester, Rochester NY.

Primary Source(s) of Research Funding: National Science Foundation (Grants No. EFMA-1641099, ECCS-1810169, and ECCS-1842691); Defense Threat Reduction Agency, Joint Science and Technology Office for Chemical and Biological Defense Grant No. HDTRA11810047; Defense Advanced Research Projects Agency (DARPA) Agreement No. HR00112090012

Contact(s): qiang.lin@rochester.edu, usman.javid@rochester.edu, jling8@ur.rochester.edu, mli53@ur.rochester.edu, yhe26@ur.rochester.edu

Primary CNF Tools Used: JEOL 9500, AJA ion mill, CVC SC4500 odd-hour evaporator

Abstract:

Integrated photonic devices have shown great promise in scalable implementation of quantum technologies for applications in information processing, communication, computing, metrology, and sensing. Particularly, for applications in metrology and sensing, a broadband source of quantum entanglement is desired. To that end, we demonstrate an integrated source of entangled photon pairs with record-high bandwidth and efficiency not seen on chip-scale platforms before. This source is fabricated on thin-film lithium niobate-on insulator wafer at the Cornell NanoScale Facility.

Summary of Research:

One of the most widely used methods to generate quantum entanglement in light is by using a nonlinear optical process called spontaneous parametric down conversion (SPDC). In this process, a laser photon spontaneously breaks into two daughter photons inside a nonlinear optical material, which are entangled in time and energy [1]. The efficiency of this process and its bandwidth is determined by the dispersion of the material used in the interaction. Efforts to generate this entanglement over a broad spectral region is primarily confined to bulk materials where the control over material dispersion is severely limited. Due to this, the only feasible method of increasing the bandwidth is to create inhomogeneity in the medium [2,3]. This severely reduces the generated spectral brightness of the photons creating a tradeoff between brightness and bandwidth of the source [2,4]. Nanophotonics, on the other hand, does not have any such limitation since the wavelength-scale geometry of thin-film devices can be exploited for precise control of the refractive index. Here, we are reporting on fabrication of a nanophotonic waveguide on thin-film lithium niobate-on-insulator wafer (LNOI), which has been engineered to produce an entanglement bandwidth exceeding 100 terahertz (THz).

The waveguide is designed for 600 nm thick lithium niobate film with X-cut orientation of the crystal axis. In order to produce a broad parametric down-conversion spectrum, the dimensions of the waveguide are engineered to have zero

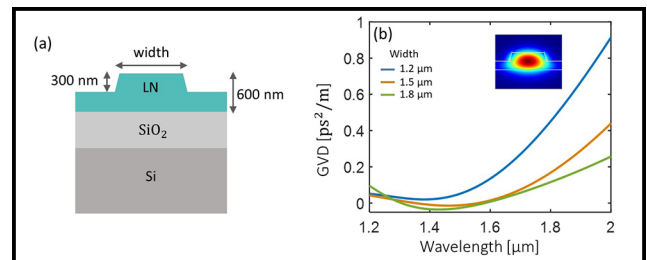


Figure 1: (a) Geometry of the lithium niobate waveguide on a 600 nm LNOI wafer. (b) Group velocity dispersion (GVD) of the waveguide at different widths with the inset showing the fundamental quasi-TE mode of the waveguide at a 1550 nm wavelength.

group velocity dispersion (as shown in Figure 1) at an optical wavelength of 1550 nm, which will form the center of the generated spectrum. The resulting waveguide has a width of 1.5 μm and an etch depth of 300 nm. The waveguide is subsequently patterned on the wafer using electron-beam lithography on the JEOL 9500 using ZEP520A as the resist mask for the waveguide.

After development, the waveguide is etched using argon ion milling on the AJA ion mill achieving a 50% (300 nm) etching depth. The resist is then stripped using standard resist remover chemistry and the chip is prepared for a second electron-beam exposure. This is to pattern electrodes on both

sides of the waveguide so that the material can be poled by applying high voltage electrical pulses that permanently alter the material's optic axis. This is done to bridge the refractive index gap between the pump laser photons, which are at a wavelength of 775 nm to the generated photon pairs which are centered at 1550 nm. The material is coated with PMMA resist and exposed again with electron-beam lithography to pattern the electrodes. After development, the chip is deposited with a 400 nm layer of gold using an evaporator (CVC SC4500). The electrode pattern is subsequently created by a resist liftoff process.

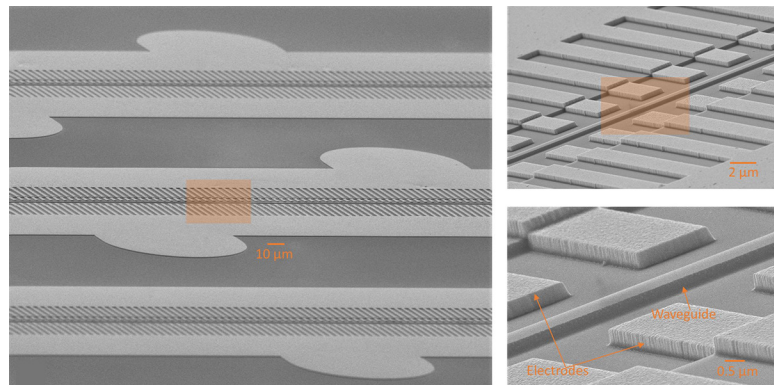


Figure 2: SEM images of a fabricated device at different magnifications.

Figure 2 shows scanning electron microscope images of a fabricated device.

After fabrication, the waveguide is pumped by a laser with a tunable wavelength. The laser wavelength is scanned, and the generated photon pairs are detected using superconducting single-photon detectors. At 770.4 nm, we observe a parametric down-conversion spectrum spanning from the central wavelength of 1540.8 nm all the way to 1100 nm as shown in Figure 3(a), giving a half spectral-width at half maximum of 50 THz (300 nm).

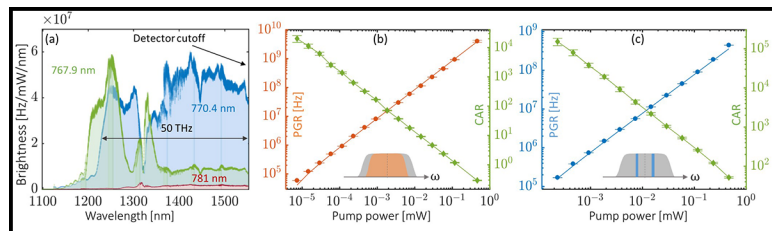


Figure 3: (a) Measured spectrum of the generated photon pairs at different pump wavelength with the blue curve plotting the highest (100 THz) bandwidth. The pair generation rate (PGR) and coincidence-to-accidental ratio (CAR) are plotted for the full spectrum in (b) and a 20 nm filtered section in (c).

The full spectrum is then expected to span up to 2000 nm, given the symmetry of the interaction, giving a total bandwidth of 100 THz. This is more than an order of magnitude larger than a typical chip-scale SPDC source. The device also shows a high efficiency of 13 GHz/mW of pump power, owing to such a large bandwidth and strong confinement of light as expected of a wavelength-scale device.

Another important metric of an entangled photon source is its signal-to-noise ratio, also known as coincidence-to-accidental ratio (CAR), which determines its performance in communication and computing applications. Figure 3(c) plots this measurement for a 20 nm filtered section of the spectrum. This is done to counter dispersive effects in the experimental setup to get the true noise characteristics. We observe a highest CAR of 152,000 the highest achieved for any chip-scale photon-pair source to date [5,6], indicating excellent noise performance, even at high pair generation rates. Additional measurements to verify quantum entanglement in the generated light are also done (not shown here) to verify our claims.

Conclusions:

To conclude, we have designed and fabricated an efficient waveguide source of ultra-broadband entangled photons. The large bandwidth of entanglement produced from this device along with its record efficiency and noise performance make such nanophotonic sources ideal for applications in quantum communication and computing.

Furthermore, we envision that this demonstration will motivate experiments in chip-scale metrology and spectroscopy with non-classical light.

References:

- [1] Reports on Progress in Physics 66.6 (2003): 1009.
- [2] Physical review letters 100.18 (2008): 183601.
- [3] Optics express 20.23 (2012): 25228-25238.
- [4] European Quantum Electronics Conference. Optical Society of America, 2019.
- [5] Physical review letters 124.16 (2020): 163603.
- [6] Optics Express 25.26 (2017): 32995-33006.

Narrow Linewidth, Widely Tunable Integrated Lasers from Visible to Near-IR

CNF Project Number: 2364-15

Principal Investigator(s): Michal Lipson

User(s): Xingchen Ji, Mateus Corato-Zanarella

Affiliation(s): Department of Electrical Engineering, Columbia University, New York City, NY 10027

Primary Source(s) of Research Funding: Defense Advanced Research Projects Agency

Contact(s): ml3745@columbia.edu, xj53@cornell.edu

Primary CNF Tools Used: PECVD, e-beam lithography, Oxford 100 etcher, AJA sputter deposition, mask writer, furnace, Oxford 82 etcher

Abstract:

We demonstrate a chip-scale platform for narrow-linewidth lasers, tunable across the whole spectrum from blue to near-IR. We show powers up to 10 mW, intrinsic linewidth less than 8 kHz, tuning up to 12 nm and high side-mode suppression ratio up to 38 dB.

Summary of Research:

Integrated photonics platforms for light sources in the visible range are promising for applications including trapping, quantum photonics [1], biosensors [2], and spectroscopy. To date, narrow linewidth, tunable visible sources either rely on bulky external free-space cavities and components [3] or are limited to the long wavelength portion of the spectrum (red) and have large footprint [4].

Here, we demonstrate a chip-scale laser platform designed for lasing with narrow linewidth and tunability over a large spectral range covering the whole visible spectrum up to near-IR. We design the platform to be based on high confinement, high quality factor (Q) silicon nitride (Si_3N_4) resonators and commercially available Fabry-Perot (FP) laser diodes. We leverage the large transparency window of Si_3N_4 for high confinement low-loss light propagation at visible wavelengths and commercial FP laser diodes for robust self-injection locking [5]. We show that by coupling laser diodes to a low-loss ring resonator with an optical feedback path, self-injection locking causes the collapse of the multiple longitudinal modes of the diode into a single longitudinal mode, with further linewidth reduction induced by the high Q of the resonator. We achieve lasing at different wavelengths by tuning the resonator's resonance to align to different longitudinal modes of the laser.

We design our photonic components to operate over the whole visible to near-IR spectral range using a platform of 175 nm-thick Si_3N_4 waveguide core surrounded by silicon oxide (Figure 1a). We design a ring resonator with tapered dimensions from 300 nm to 1500 nm to ensure near-single mode operation and good coupling for all the wavelengths while maintaining high Q (Figure 1b) [6]. We leverage the high confinement to design the ring with small radius (10 μm). The resulting large free-spectral range (FSR)

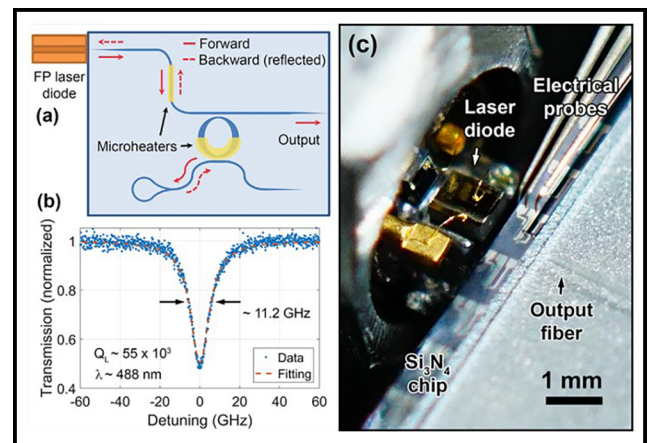


Figure 1: (a) Schematic of the integrated laser. An FP laser diode is butt-coupled to the chip, where a ring resonator with a feedback loop at the drop port acts as a wavelength selective reflector. (b) Ring resonance in blue measured with a Toptica DL Pro 488 nm laser. The loaded quality factor is $\sim 5.5 \times 10^4$ and the extinction is $\sim 50\%$. (c) Image of the laser setup.

of several nm across the whole visible range allows the feedback of a specific wavelength within the gain bandwidth of the laser diodes without the need for a Vernier filter [4]. Such a frequency-selective feedback over a large range eliminates mode-hopping between longitudinal modes of the laser diodes when they are self-injection locked by our resonator. The feedback wavelength can be continuously tuned within the FSR by tuning the resonator. We optimize the feedback loop at the drop port for broad bandwidth, leveraging that the self-injection locking of FP laser diodes is robust to the amount of reflection [5]. We design inverse taper edge couplers to provide good laser-to-chip and chip-to-fiber coupling without inducing spurious reflections.

We achieve broadband, narrow linewidth, tunable lasing by butt-coupling commercial FP laser diodes to our chip and

controlling the position of the ring resonator's resonance using thermo-optic phase shifters (Figure 1c). We tune the lasing wavelength by tuning the resonator to different longitudinal modes of the laser diodes. When the resonator is detuned from the modes of the laser, the power dropped to the feedback loop is negligible and the laser diode lases with multiple longitudinal modes (Figure 2a). When we align the resonator to a mode of the laser, power is dropped to the feedback loop and then reflected back to the diode. We adjust the phase of the reflected light to cause the self-injection locking by using the phase-shifter on the bus waveguide in between the diode and the resonator. When the laser is locked, the longitudinal modes of the laser diode collapse into a single one (Figure 2b).

We show narrow linewidth, tunable integrated lasers covering blue (~492 nm), green (~522 nm), red (~660 nm) and near-IR (~785 nm) wavelengths with output fiber-coupled powers up to 10 mW, intrinsic linewidth < 8 kHz, wavelength tuning up to 12 nm and side-mode suppression ratios (SMSR) up to ~38 dB. We achieve coarse tuning ranges/SMSRs of ~3.21 nm/~30 dB in blue, ~3.2 nm/~30 dB in green, ~3.7 nm/~37 dB in red, and ~12 nm/~38 dB in near-IR (Figure 3).

We measure the intrinsic linewidths at the two extremes of the spectrum, blue and near-IR, and obtain (8 ± 2) kHz and (601 ± 227) Hz respectively, both limited by our instruments. We determine the linewidth in blue by measuring the RF beat note between our integrated laser and a commercial narrow-linewidth laser using a spectrum analyzer. The beat note represents the lineshape of our integrated laser, limited by the lineshape of the commercial laser. By fitting the beat note with a Voigt profile, we extract the Lorentzian contribution, which corresponds to the white noise that defines the intrinsic linewidth, and the Gaussian contribution, which corresponds to the flicker and technical noises that broaden the effective linewidth. The Voigt fitting of the lineshape (see Figure 4a) gives an intrinsic (Lorentzian) linewidth of (8 ± 2) kilohertz and a Gaussian linewidth of (250 ± 20) kilohertz. We measured the lineshape and frequency noise of our integrated near-IR laser with a linewidth analyzer. The Voigt fittings of the lineshapes (see Figure 4b) for different measurements give an intrinsic linewidth of (601 ± 227) hertz, limited by the linewidth analyzer sensitivity.

Our results show that chip-scale visible lasers can exhibit key specifications such as linewidth, tuning range, power, and SMSR comparable to bulky commercial laser systems. We envision our platform to be a key enabler for fully integrated visible light systems in applications including quantum photonics, trapping, AR/VR, biosensing, atomic clocks, and spectroscopy.

References:

- [1] R. J. Niffenegger, et al., "Integrated multi-wavelength control of an ion qubit," *Nature*, vol. 586, no. 7830, Art. no. 7830, Oct. 2020, doi: 10.1038/s41586-020-2811-x.
- [2] A. Mohanty, et al., "Reconfigurable nanophotonic Si probes for sub-millisecond deep-brain optical stimulation," *NatBiomedEng*, V4, #2, Art. #2, 2/20, doi: 10.1038/s41551-020-0516-y.
- [3] P. S. Donvalkar, et al., "Self-injection locked blue laser," *J. Opt.*, vol. 20, no. 4, p. 045801, Feb. 2018, doi: 10.1088/2040-8986/aae4f.
- [4] C. A. A. Franken, et al., "A hybrid-integrated diode laser for the visible spectral range," *ArXiv201204563 Phys.*, Dec. 2020, Accessed: Apr. 07, 2021. Available: <http://arxiv.org/abs/2012.04563>.
- [5] A. Gil-Molina, et al., "Robust Hybrid III-V/Si₃N₄ Laser with kHz-Linewidth and GHz-Pulling Range," in *Conference on Lasers and Electro-Optics (2020)*, paper STu3M.4, May 2020, p. STu3M.4, doi: 10.1364/CLEO_SI.2020.STu3M.4.
- [6] M. Corato-Zanarella, et al., "Overcoming the Trade-Off Between Loss and Dispersion in Microresonators," in *Conference on Lasers and Electro-Optics (2020)*, paper STh1J.1, May 2020, p. STh1J.1, doi: 10.1364/CLEO_SI.2020.STh1J.1.

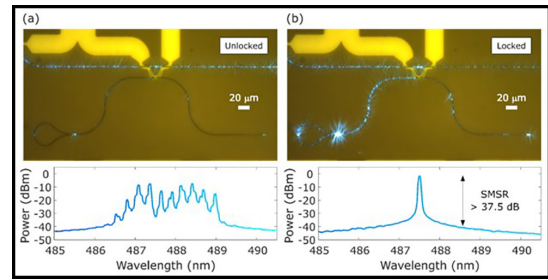


Figure 2: Microscope images of the ring resonator-based feedback loop and optical spectra of the chip output before and after self-injection locking. (a) Ring resonance is detuned from the Fabry-Perot (FP) laser diode modes, so no light is in the feedback loop (top). The chip output resembles the usual output of the FP laser with multiple lasing modes. (b) Ring resonance is tuned to one of the FP modes, so the feedback loop reflects part of the light back to the diode. Self-injection locking causes all the longitudinal modes to collapse into a single frequency, narrow linewidth lasing mode with high (> 37.5 dB) side mode suppression ratio (SMSR). The optical spectra are measured with an optical spectrum analyzer (Ando AQ6314A).

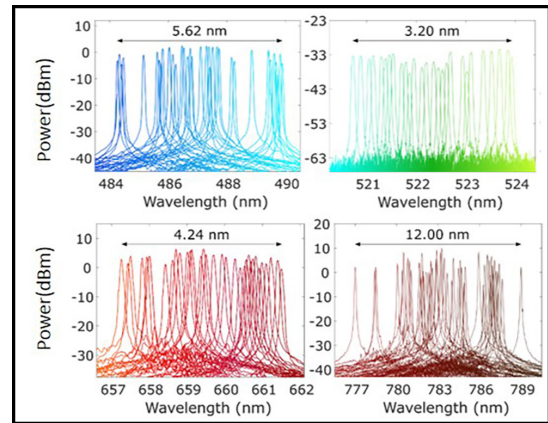


Figure 3: Coarse tuning ranges at blue, green, red and near-IR. The optical spectra are measured with an optical spectrum analyzer (Ando AQ6314A) and overlaid to show the tuning.

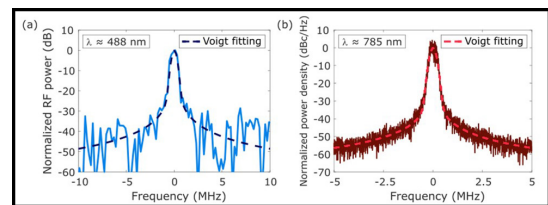


Figure 4: Linewidth characteristics of the blue and near-IR integrated lasers. RF beat note between our integrated blue laser and a commercial narrow-linewidth blue laser (Toptica DL Pro 488 nm). The beat note represents the lineshape of our integrated laser, limited by the lineshape of the commercial laser. By fitting the beat note with a Voigt profile, we extract the Lorentzian contribution, which corresponds to the white noise that defines the intrinsic linewidth, and the Gaussian contribution, which corresponds to the flicker and technical noises that broaden the effective linewidth. The Voigt fitting results in an intrinsic (Lorentzian) 8 ± 2 kHz linewidth and Gaussian linewidth of 250 ± 20 kHz.

Development of Single and Double Layer Anti-Reflective Coatings for Astronomical Instruments

CNF Project Number: 2458-16

Principal Investigator(s): Gordon Stacey¹

User(s): Bugao Zou², Nicholas Cothard²

Affiliation(s): 1. Department of Astronomy (Stacey), 2. Department of Applied and Engineering Physics; Cornell University

Primary Source(s) of Research Funding: NASA Grant NNX16AC72G

Contact(s): stacey@cornell.edu, bz332@cornell.edu, nc467@cornell.edu

Primary CNF Tools Used: Oxford PECVD, Anatech resist strip, Oxford 81/82 etcher, Oxford 100 etcher, manual resist spinners, resist hot strip bath, Plasma-Therm deep silicon etcher, ASML 300C DUV stepper

Abstract:

We have been developing silicon-substrate based mirrors for Fabry-Perot Interferometers (FPI) for astronomical instruments in the mid-infrared to sub-mm/mm wavelength regime. The mirrors are patterned with double-layer metamaterial anti-reflection coatings (ARC) on one side and metal mesh reflectors on the other side. The double-layer ARC ensures a reflectance of less than 1% at the surface substrate over the FPI bandwidth.

Summary of Research:

The goal of the project is to develop microfabricated, silicon-substrate based mirrors for use in cryogenic Fabry-Perot Interferometers for astronomical instruments in the mid-infrared to sub-mm/mm wavelength regimes. The mirrors consist of high-purity, float-zone, 500- μm -thick silicon wafers that are lithographically patterned with frequency-selective, gold mesh reflectors. We use a combination of inductive and capacitive meshes to maintain uniform high reflectance and hence nearly uniform resolving power over the FPI bandwidth. Due to the high index of refraction of silicon, the other side of the mirror must be patterned with an ARC to achieve broadband capability and to mitigate contaminating resonances from the silicon surface [1,2].

The bulk of our work this year has been the development of the fabrication methods of the ARC. Figure 1 shows our current recipe for a two-layer ARC.

A scanning electron microscope (SEM) image of the cross section of the ARC is shown in Figure 2. We are currently working to improve our control of this method. In addition, our fabrication process for metal mesh reflectors has been improved over this past year. We have successfully deposited 10-micron scale capacitive and inductive gold meshes on samples using AZ nLOF 2020 photoresist and the CHA evaporator. The lift-off procedure is done using heated Microposit 1165 Remover.

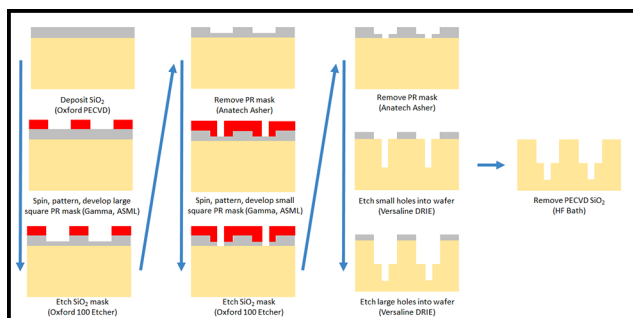


Figure 1: Process flow for fabricating a double-layer ARC on Si wafer.

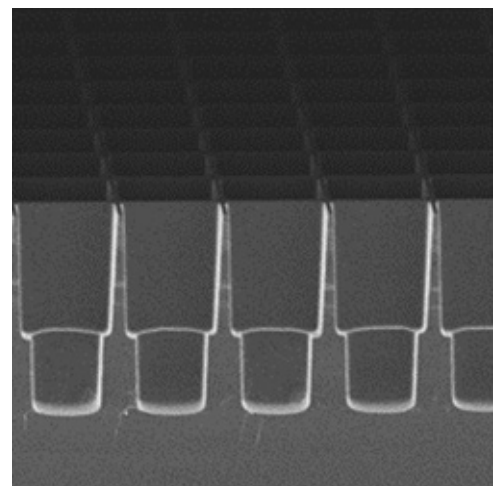


Figure 2: CNF Zeiss Ultra SEM image showing the two-layer structure of anti-reflection coatings.

We have fabricated both ARC and metal mesh reflectors on several optical quality silicon wafers and are now measuring their frequency dependent transmittances in the mid-infrared to sub-mm/mm wavelength regimes using Fourier transform spectrometers. Our progress on these devices is discussed in a paper published in Journal of Low Temperature Physics, which illustrates the design of the CCAT-prime Epoch of Reionization Spectrometer instrument and how the microfabricated FPI fits in the module and enables spectroscopic observations of the early universe [1].

The silicon-substrate based mirrors that are developed in CNF will be used in the upcoming scanning FPI instrument Prime-Cam in the CCAT-prime observatory, which is located at 5600 meters elevation on Cerro Chajnantor in the Atacama Desert in Chile [3]. CCAT-prime will use our FPI for one of its main science goals, that is to study the Epoch of Reionization of the universe via [CII] intensity mapping in the 750-1500 μm regime. Our instrument will enable the intensity mapping observations by providing high-sensitivity, wide-field, broadband spectroscopy. These measurements will tell us about how the first stars and galaxies evolved in the early universe.

Conclusions and Future Steps:

In the past year we have made great steps towards achieving our goals at CNF. We have demonstrated our ability to fabricate double-layer ARCs for different wavelengths and metal meshes with different feature sizes. We have used many of the fabrication and metrology tools at CNF. Our next steps are to better characterize our etched geometries and improve our metamaterial ARCs. We will be using Fourier transform spectrometers to measure our sample's optical performance and using the results to iterate on our fabrication design.

References:

- [1] Cothard, N.F., Choi, S.K., Duell, C.J., et al. The Design of the CCAT-prime Epoch of Reionization Spectrometer Instrument. *J Low Temp Phys* (2020). <https://doi.org/10.1007/s10909-019-02297-1>.
- [2] N.F. Cothard, M. Abe, T. Nikola, G.J. Stacey, G. Cortes-Medellin, P.A. Gallardo, B.J. Koopman, M.D. Niemack, S.C. Parshley, E.M. Vavagiakis, and K. Vetter, "Optimizing the efficiency of Fabry-Perot interferometers with silicon-substrate mirrors," *Adv. in Optical and Mechanical Tech. for Telescopes and Instrumentation III* (2018).
- [3] <http://www.ccatobservatory.org/>

Electrically Actuated Zoom-Lens Based on a Liquid-Crystal-Embedded Semiconductor Metasurface

CNF Project Number: 2472-16

Principal Investigator(s): Gennady Shvets

User(s): Melissa Bosch, Maxim Shcherbakov

Affiliation(s): School of Applied and Engineering Physics, Department of Physics; Cornell University

Primary Source(s) of Research Funding: Office of Naval Research (ONR), National Science Foundation (NSF)

Contact(s): gs656@cornell.edu, mb2583@cornell.edu, mrs356@cornell.edu

Website: <http://shvets.aep.cornell.edu>

Primary CNF Tools Used: JEOL 9500, Zeiss Ultra SEM, Oxford Cobra ICP etcher, Oxford PECVD

Abstract:

Planar metamaterials, or metasurfaces, offer an ultrathin and adaptable platform for modulating spatial and spectral properties of light. We engineer semiconductor-based metasurfaces which exhibit tunable optical resonances for photonic applications in near-infrared. We report on the design, fabrication, and characterization of resonant amorphous silicon (a-Si) metasurfaces that act as a voltage-tunable dynamic-focus lenses likely to find uses in augmented reality and other imaging technologies.

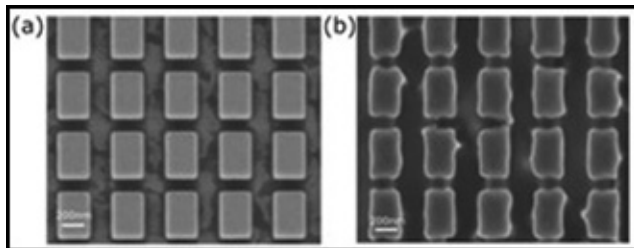


Figure 1: (a) A scanning electron microscope image of a typical a-Si-based resonant metasurface on an ITO-coated SiO_2 substrate. (b) Same as (a), but before improving the fabrication process.

Summary of Research:

Fabrication of a-Si Metasurfaces. Metasurfaces present a compact and scalable alternative to conventional free-space optical elements. Dielectric and semiconductor metasurfaces, such as those consisting of germanium or silicon, can generate near-arbitrary spatial phase profiles with low absorptive losses, leading to high-performance waveplates, beam deflectors, and lenses with subwavelength-thickness [1]. Our project focuses on the design and fabrication of resonant amorphous silicon (a-Si) metasurfaces with sub-100 nm feature sizes and high (up to 1:6) aspect ratios, useful for numerous applications where compact and efficient light modulators are sought. Figure 1a shows a representative a-Si metasurface, consisting of an array of rectangular a-Si prisms patterned on a fused silica substrate. Such regular semiconductor nanoarrays support

localized electric and magnetic Mie-type resonant optical modes, which may be spectrally-tuned by modifying the permittivity of the media (e.g., liquid crystals: LC) adjacent to the array. The metasurface fabrication consisted of six steps: plasma-enhanced chemical vapor deposition (Oxford PECVD) of a-Si onto an ITO-coated fused silica substrate and surface treatment with SurPass 3000 adhesion promoter; standard HSQ 6% spin-coat, baking, and e-beam exposure at 6 mC/cm^2 (JEOL 9500FS); development in TMAH/NaCl (0.25/0.7N) salty solution; and pattern transfer to the a-Si layer through an inductively coupled HBr plasma reactive ion etch (Oxford Cobra). The resulting samples were characterized with a scanning electron microscope (Zeiss Ultra). The resulting structures show excellent accuracy in geometric dimensions, a significant improvement over our first-generation metasurfaces produced with MIF300 developer (Figure 1b).

Tunable-Focus Lens Based on a Liquid-Crystal-Embedded a-Si Metasurface. In one application, we apply a-Si metasurfaces towards the design of metalenses with tunable focal lengths. Compact lenses with adjustable focal lengths are essential to modern imaging technologies such as adaptive vision devices and wearable augmented reality displays; however, most metalenses exhibit static functionalities post-fabrication. Our work uses a-Si metasurfaces infiltrated with liquid crystals (LCs) to demonstrate a varifocal metalens with voltage-actuated focal length [2]. This is accomplished through the design of a resonant a-Si metasurface encapsulated in a LC cell. The latter behaves as an anisotropic dielectric medium with

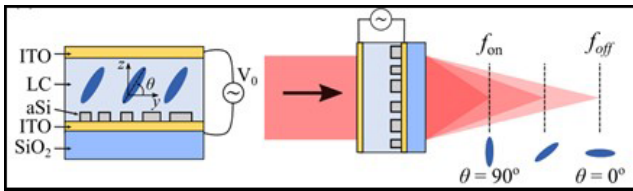


Figure 2: Schematic of the device. Left: A silicon-based metalens is encapsulated in a liquid crystal cell between two transparent conducting oxide electrodes. An AC voltage is applied to the electrodes, driving the orientation of the LC molecules at angle θ with respect to y . Right: Illustration depicting the θ -dependent focal length of light transmitted through the metalens.

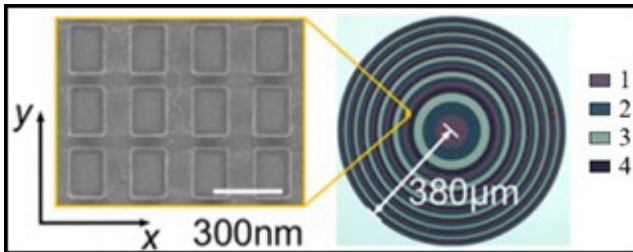


Figure 3: Left: A SEM image of the first metalens subzone. Right: Optical microscope image of the fabricated spherical metalens. The different shades of the metalens correspond to its four different metasurface geometries.

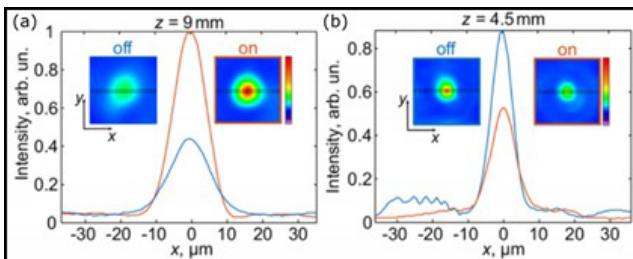


Figure 4: Experimental voltage-dependent focal spot profiles of the metalens (a) Intensity linecuts of the $z = 9$ mm focal spot image at the 'off' and 'on' voltages of $2.2V_{pp}$ and $9.8V_{pp}$, respectively. The insets show the respective camera images. (b) Same as (a), but for $z = 4.5$ mm.

voltage-dependent optical axis orientation angle θ of the LC molecules, as depicted in Figure 2. The metalens exploits the electro-optic properties of LCs to tailor the local phase response of the silicon meta-atoms, resulting in continuous and reversible modulations of the metalens focal length.

For the design of a switchable-focus LC metalens, we present a metasurface unit cell template consisting of rectangular silicon pillars encapsulated in a nematic LC between two conductive plates, as shown in Figure 2. The meta-atom geometries are optimized to impart phase shifts to achieve the required hyperbolic phase profile for a spherical lens with focal distance $f = f_{off}$ for $\theta = 0^\circ$, while simultaneously engineered to impart the phase profile of a lens with $f = f_{on}$ for $\theta = 90^\circ$. Therefore, this selection enables voltage-controlled switching between two discrete focal distances of the lens.

We validate this concept by designing and fabricating a 2D metalens that emulates a transition between two distinct concave lenses with focal lengths of $f_{off} = 9$ mm and $f_{on} = 4.5$ mm, respectively. Figure 3 shows an SEM image of the fabricated lens. The experimental focal spot tuning is shown in Figure 4. By increasing the AC voltage bias across the LC cell from $2.0V_{pp}$ ('off') to $9.8V_{pp}$ ('on'), the focal spot intensity increases by 58% at $z = f_{on}$ and decreases by 37% at $z = f_{off}$.

References:

- [1] Soref, Richard. "Mid-infrared photonics in silicon and germanium." *Nature photonics* 4.8 (2010): 495.
- [2] Bosch, M., Shcherbakov, M. R., Won, K., Lee, H. S., Kim, Y., and Shvets, G. "Electrically actuated varifocal lens based on liquid-crystal-embedded dielectric metasurfaces". *Nano Letters* 21.9 (2021): 3849-3856.

Lithium Niobate Ring Resonator Device for Adiabatic Wavelength Conversion

CNF Project Number: 2524-17

Principal Investigator(s): Jaime Cardenas

User(s): Xiaotong He

Affiliation(s): The Institute of Optics, University of Rochester

Primary Source(s) of Research Funding: National Science Foundation

Contact(s): jaime.cardenas@rochester.edu, xhe20@ur.rochester.edu

Website: <https://www.hajim.rochester.edu/optics/cardenas/>

Primary CNF Tools Used: JEOL 9500, AJA ion mill, Oxford 100 PECVD, Plasma-Therm 72 and 740 etchers, AJA sputter deposition, CVC SC4500 evaporator, Zeiss SEM, Xactix xenon difluoride etcher, ABM contact aligner, Heidelberg mask writer - DWL2000, DISCO dicing saw

Abstract:

We are working on a brand-new method to change the frequency of light after its emission from laser by applying an electrical signal to ring resonators. Such a novel device will get rid of an optical pump or a gain medium in nonlinear frequency conversion.

Summary of Research:

Changing the frequency of light outside the laser cavity is typically done by nonlinear process like four wave mixing. However, integrating a system with high power optical pump into a photonic chip is a challenge. To achieve on-chip optical frequency conversion, we are working on a method of electrically tuning of ring resonator to go through adiabatic wavelength conversion. With this technique, we can dynamically control light in cavity within photon lifetime by tuning coupling between ring resonators electrically. Moreover, such a novel device will simplify and compact telecommunication components like wavelength-division multiplexing (WDM) with single frequency light input.

In previous work, adiabatic wavelength conversion (AWC) is achieved in silicon ring resonators [1-3] by using strong optical pumps incident on the cavity from above the chip. Similar to tuning frequency of sound by changing the length of the string, we can do the same to light wave by modulating the refractive index of the cavity. The light trapped inside the cavity shifts its frequency with resonance shift of the resonator. In silicon platform, the optical pump is absorbed and generates free carriers, which causes a change in the refractive index of the cavity. However, AWC in silicon introduces an optical loss, which reduces the photon lifetime and limits the conversion efficiency. It also requires a femtosecond timescale high power pulsed laser, which limits the scalability of AWC platform.

We are developing a method for electrical frequency conversion on a lithium niobate on insulator (LNOI) integrated photonic platform, the existence of which enables ultra-high quality resonators for long photon lifetime.

Besides, lithium niobate has a large electro-optic effect and allows instantaneous changes in the refractive index, making it an ideal material for electrical AWC.

The LNOI sample we use consists of 600 nm thick lithium niobate (LN), 4.7 μm thick thermal SiO_2 bottom isolation layer and 0.5 mm thick silicon handle. We deposit electron-beam resist maN-2405 on the top of the sample with Surpass 4000 as adhesion. Ring resonators and waveguides are patterned with e-beam lithography process. Lithium niobate is usually etched physically with argon ions to avoid the non-volatile lithium fluoride byproducts shown in fluorine based etching techniques [4]. We etch 350 nm of LN in AJA ion mill and left a 250 nm LN slab. The resist is stripped with oxygen plasma in the PT72 etcher. However, we found that oxygen plasma can hardly remove the micro-masking formed by the interaction between argon and resist. Hence, we put the sample in RCA-1 silicon wafer cleaning process for 45 min to fully remove the residue on the sidewall. We check the sample with a scanning electron microscope (SEM) to make sure that micro-masking is completely removed before further moving on.

After the waveguide pattern is defined, we deposit a thin layer of SiO_2 with plasma-enhanced chemical vapor deposition (PECVD) to protect the waveguides. To pattern the bottom electrodes besides the waveguide, we deposit double layered PMMA and went through another e-beam process, which ensures a tolerance within tens of nanometers. We chose an evaporator as the metallization method to deposit Pt with Cr as an adhesion layer, which can further reduce the production of debris.

After an overnight lift-off, we deposit $2\ \mu\text{m}$ SiO_2 with PECVD. Via holes are patterned with contact aligner and etched with a CHF_3/O_2 recipe of PT72 to expose the bottom electrodes. Top electrodes, designed to be bridges connecting two bottom electrodes and serve as contact pads to probes, are also patterned with contact aligner because the tolerance can be up to several microns. The AJA sputter tool is needed because the sidewalls of the via holes have to be covered or it will be an open circuit. And then a second lift-off process is proceeded.

We found that the top cladding oxide will break and fall off when the dicing saw goes through it, making the input coupling fairly poor. We also tried polishing, but realized that it's not easy for a holder to clamp a 1 mm wide chip. As a result, we tried to use etching method to get smooth facets. The facet is also patterned with contact aligner. Before the dicing, we used PT740 to etch the top and bottom SiO_2 cladding as well as LN slab with ion mill. After the dicing process, chips are put into the xenon difluoride etcher to undercut the silicon substrate.

We test the spectrum of the ring resonators we produced. It shows the loaded quality factor of around 100k, which corresponds to intrinsic quality factor of 170k. We also applied voltage to the device to test the electro-optics efficiency. As shown in Figure 1, the blue curve is the original spectrum without voltage applied. Red and yellow ones are the spectrum when we apply positive and negative 30V. It shows that the electro-optic efficiency is around 7pm/V. These results meet the criteria for an AWC device. We are now working on experiments to get the wavelength converted signal.

Conclusions and Future Steps:

We fabricated devices that show possibility for electrical AWC. We are now working on the experiments to get the

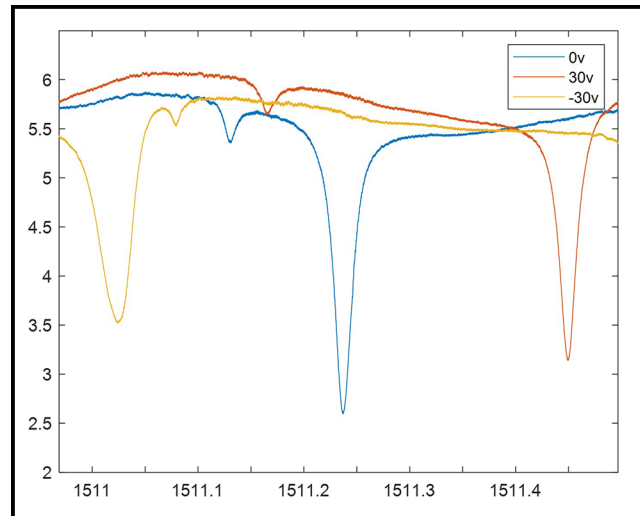


Figure 1: Spectrum of ring resonator when applying voltage.

wavelength converted signal. In the future, we will try to improve the quality factor and electro-optical efficiency of the devices.

References:

- [1] Preble S F, Xu Q, Lipson M. Changing the color of light in a silicon resonator. *J. Nature Photonics*, 2007, 1(5):293-296.
- [2] Daniel B A, Maywar D N, Agrawal G P. Efficient adiabatic wavelength conversion in Gires-Tournois resonators. *J. Optics Letters*, 2011, 36(21):4155.
- [3] B. A. Daniel, D. N. Maywar, and G. P. Agrawal, *J. Opt. Soc. Am. B* 28, 2207 (2011).
- [4] Luke K, Kharel P, Reimer C, et al. Wafer-scale low-loss lithium niobate photonic integrated circuits. *J. Optics Express*, 2020, 28(17): 24452-24458.

Precise Phase Measurement with Weak Value Amplification on Integrated Photonic Chip

CNF Project Number: 2524-17

Principal Investigator(s): Jaime Cardenas

User(s): Meiting Song

Affiliation(s): The Institute of Optics, University of Rochester

Primary Source(s) of Research Funding: DRS, Andrew Jordan LLC

Contact(s): jaime.cardenas@rochester.edu, msong17@ur.rochester.edu

Website: <https://www.hajim.rochester.edu/optics/cardenas/>

Primary CNF Tools Used: Low pressure chemical vapor deposition (LPCVD), plasma-enhanced chemical vapor deposition (PECVD), JEOL 9500 e-beam lithography, ASML stepper, Oxford 100 inductively coupled plasma reactive ion etching (ICP-RIE), AJA sputter deposition

Abstract:

We show, for the first time, phase measurement with weak value amplification on an integrated photonic chip. We demonstrate 9 dB improvement of signal over an on-chip Mach-Zehnder interferometer with equal amount of detected optical power.

Summary of Research:

Weak value amplification has shown the ability to make sensitive measurements with a small portion of the light signal, including beam deflection measurement of 400 frad with $63 \mu\text{W}$ out of 3.5 mW light power [1], frequency sensitivity of $129 \text{ kHz}/\sqrt{\text{Hz}}$ with $85 \mu\text{W}$ out of 2 mW [2] and temperature sensor with 4-fold enhancement [3]. By introducing a perturbation and post-selection of the light, weak value can amplify the interferometric signal without amplifying the noise, resulting in a higher signal-to-noise ratio (SNR). Therefore, in a detector saturation limited system, weak value amplification can further increase the SNR. However, tabletop setups are space consuming and vulnerable to environmental changes. By taking this technique to the integrated photonics regime, we can largely improve its robustness and compactness, making it a good candidate for precision metrology.

We used an integrated Mach-Zehnder interferometer (MZI) followed by a multi-mode interference waveguide (MMI) (Figure 1) to achieve inverse weak value measurement. For traditional weak value amplification in optical interferometers, a propagation phase shift between the two paths is introduced to amplify spatial phase front tilt signal introduced by a tilted mirror. However, in integrated photonics, sensing is usually achieved with propagation phase. Therefore, we apply “inverse” weak value amplification (IWVA), which uses spatial phase front tilt to amplify propagation phase signal. To introduce a spatial phase tilt in a waveguide, we designed the mode converter in Figure 1 to couple a small part of the light from TE_0 mode to TE_1 . This is based on that the Hermite-Gaussian (HG) expansion of free space IWVA output beam is mainly a combination of HG_0 and HG_1 modes [4]. Since eigenmodes of a waveguide are similar to Hermite-Gaussian modes, we applied the theory on waveguide eigenmodes TE_0 and TE_1 .

We design a multimode coupler to couple light from fundamental mode to higher order mode. As shown in Figure 1 (between dashed lines), the straight branch is a single mode waveguide which transits to a multimode waveguide through an adiabatic taper. Therefore, TE_0 mode in the lower waveguide stays in TE_0 mode. The bending branch couples a slight portion of light from TE_0 in lower waveguide. Then it couples back into the lower waveguide, but to TE_1 mode, since the TE_1 mode supported by the multimode waveguide is designed to be phase matched with TE_0 in the bending branch.

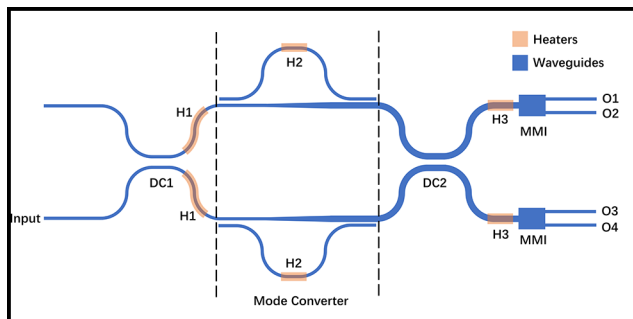


Figure 1: Layout of the device with heaters (not to scale). DC: directional coupler; H: heater; MMI: multi-mode interferometer; O: output.

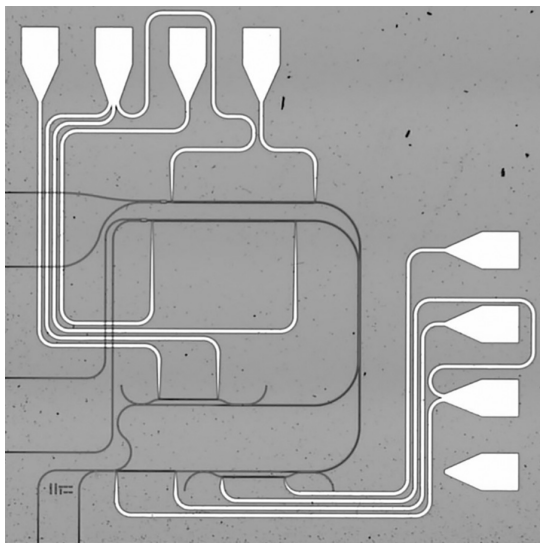


Figure 2: Microscope capture of the device. The device is wrapped around to reduce footprint.

To readout the phase shift introduced by heater 1 in Figure 1, which translates to measuring the ratio of TE_0 and TE_1 modes, we design a multimode interferometer (MMI). We used an MMI as simulation shows that its output power is dependent on the ratio of the input TE_0 and TE_1 modes.

We then fabricated the device with CMOS compatible process (Figure 2). The fabrication started with a 4-inch silicon wafer with $4\ \mu\text{m}$ of thermal grown silicon dioxide. We deposited a layer of 289 nm silicon nitride with low pressure chemical vapor deposition (LPCVD). Then we used e-beam lithography to pattern the waveguides and etched the silicon nitride with inductively coupled plasma reactive ion etching (ICP-RIE). We deposited $2.6\ \mu\text{m}$ of silicon dioxide with plasma enhanced chemical vapor deposition (PECVD).

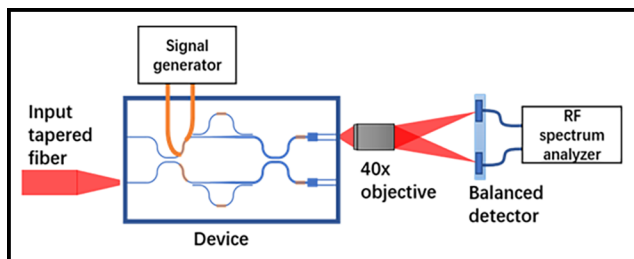


Figure 3: Illustration of testing setup.

Finally, we sputtered 100 nm of platinum, patterned with deep UV lithography, and used lift-off method to form the heaters.

We compare our weak value device with a standard on-chip MZI with same footprint working in quadrature (Figure 3). We launch 1 mW of laser power at 1570 nm with a tapered optical fiber. The phase signal is introduced by applying a modulated 1V, 10 kHz sinusoid voltage to heater 1.

The outputs of the waveguides are imaged onto a balanced detector, and we measure the signal on an RF spectrum analyzer.

We demonstrate 9 ± 1.9 dB signal improvement over the regular MZI in the weak value device with equal amount of detected optical power. When detected powers are $14\ \mu\text{W}$, weak value device has a signal of 66.17 dBm, while the regular MZI shows 75.33 dBm. For the regular MZI to also show a signal of 66.17 dBm, it requires a higher detected power of $40.5\ \mu\text{W}$.

Conclusions and Future Steps:

In conclusion, we have shown that on-chip weak value device is a good candidate for phase related metrology, including temperature drift and frequency shift. As it provides higher signal with same amount of optical power, it can monitor the optical signal in a system without consuming a large portion of the light. On the other hand, in a detector saturation limited system, weak value device is able to further increase the signal.

References:

- [1] P. B. Dixon, D. J. Starling, A. N. Jordan, and J. C. Howell, "Ultrasensitive Beam Deflection Measurement via Interferometric Weak Value Amplification," *Phys. Rev. Lett.* 102, 173601 (2009).
- [2] D. J. Starling, P. B. Dixon, A. N. Jordan, and J. C. Howell, "Precision frequency measurements with interferometric weak values," *Phys. Rev. A* 82, 063822 (2010).
- [3] L. J. Salazar-Serrano, D. Barrera, W. Amaya, S. Sales, V. Pruneri, J. Capmany, and J. P. Torres, "Enhancement of the sensitivity of a temperature sensor based on fiber Bragg gratings via weak value amplification," *Opt. Lett.*, OL 40, 3962-3965 (2015).
- [4] J. Steinmetz, K. Lyons, M. Song, J. Cardenas, and A. N. Jordan, "Precision frequency measurement on a chip using weak value amplification," in *Quantum Communications and Quantum Imaging XVII* (International Society for Optics and Photonics, 2019), Vol. 11134, p. 111340S.

Engineered Second-Order Nonlinearity in Silicon Nitride

CNF Project Number: 2524-17

Principal Investigator(s): Jaime Cardenas

User(s): Yi Zhang

Affiliation(s): The Institute of Optics, University of Rochester

Primary Source(s) of Research Funding: National Science Foundation

Contact(s): jaime.cardenas@rochester.edu, yzh239@ur.rochester.edu

Website: <https://www.hajim.rochester.edu/optics/cardenas/>

Primary CNF Tools Used: JEOL 9500, ASML PAS 5500/300C DUV stepper, Oxford PECVD, Oxford 100 etcher

Abstract:

We induce a permanent second order nonlinearity up to 26 fm/V in silicon nitride via electrical poling at a high temperature. We demonstrate electro-optic modulation on the engineered silicon nitride device up to 15 GHz.

Summary of Research:

Silicon nitride (Si_3N_4) is a low loss, CMOS-compatible material that has revolutionized many fields including integrated photonics and nonlinear optics, but the lack of a significant electro-optic response limits its applications. Second harmonic generation (SHG) [1-3] is promising; however, these platforms do not show feasible signal modulation at gigahertz or higher speed. Building an electro-optic response available for gigahertz (GHz) modulation in Si_3N_4 will create a new photonic platform with great potential in silicon photonics and quantum optics.

We propose to align the Si-N bonds in Si_3N_4 and induce an electro-optic effect by electrically poling the Si_3N_4 device. Khurgin hypothesized that the Si-N bonds in Si_3N_4 possess a second-order hyperpolarizability comparable to Ga-As bonds in gallium arsenide (GaAs) [4], whose $\chi^{(2)}$ is as large as 300 pm/V. However, the centro-symmetric structure of Si_3N_4 — meaning the bonds are oriented isotropically — leads to the absence of a second-order nonlinearity ($\chi^{(2)}$) and Pockels effect. A non-trivial $\chi^{(2)}$ will naturally emerge in Si_3N_4 if an applied force can align the bonds towards a certain direction, even by just a few degrees, and thus break the structural symmetry of the material.

The Si-N bonds are electrically asymmetric and behave as dipoles (Figure 1(a-b)). We place a pair of tantalum (Ta) electrodes 100 nm (edge-to-edge) away from the waveguide (cross section $1\ \mu\text{m} \times 300\ \text{nm}$) to provide a horizontal electric field strong enough to efficiently align the Si-N bonds (Figure 1(d)). The maximum bias we can apply before arcing happens is 200V, generating a field 1 MV/cm in the Si_3N_4 , very close to its electrical breakdown threshold.

To further enhance the poling process, we heat up the Si_3N_4 ring by focusing a 10W CO_2 laser beam at the device (Figure 1(d)) as the poling begins. The temperature reached is approximately 700°C , estimated based on the incandescent color of the device. Such high temperature makes the Si-N bonds more susceptible to the applied field. The poling lasts for five minutes before the heating laser is switched off, and the sample cools down while the poling field stays on. The rapid cooling prevents the aligned bonds from a complete reversal and ‘freezes’ them at their new positions permanently even after the removal of the poling field.

The fabrication of our device starts from depositing 300 nm of Si_3N_4 using low pressure chemical vapor deposition (LPCVD) over $4\ \mu\text{m}$ thermally grown SiO_2 on a 4-inch silicon wafer. We pattern the ring resonator using electron-beam lithography and inductively coupled plasma reactive-ion etching (ICP-RIE). The temporary Ta electrodes and another pair of permanent platinum (Pt) electrodes for high-speed modulation (Figure 1(c)) are then separately patterned using DUV photolithography and deposited by sputtering.

We examine the induced electro-optic coefficient (EOC) in our device by applying a modulation

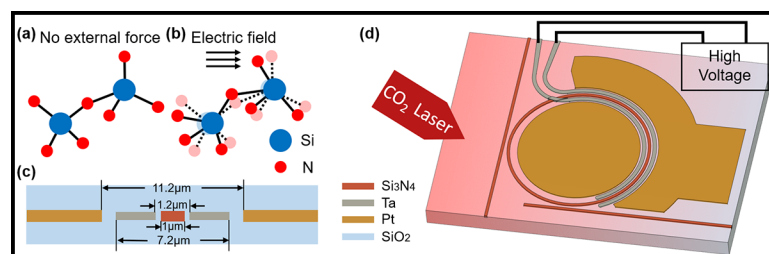


Figure 1: (a-b) Si_3N_4 lattice without (a) and with (b) an electric field applied. (c) Schematic of poling the Si_3N_4 ring with device heated by CO_2 laser. (d) Cross section of the device.

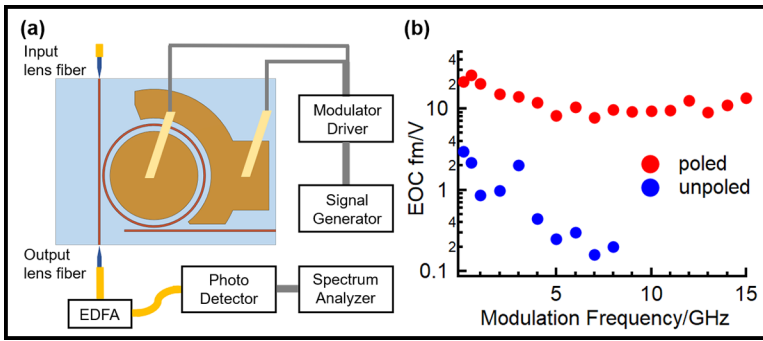


Figure 2: (a) Schematic of measuring the introduced second order nonlinearity in the Si_3N_4 ring resonator. (b) Measured r_{zzz} versus modulation frequency.

signal on it and examine its performance. As shown in Figure 2(a), a signal generator sends modulation signal, amplified by a modulator driver, to the Pt electrodes sandwiching the ring (Ta electrodes removed by XeF_2 etching) through a pair of micro probes. We set the working wavelength properly so that the modulation efficiency is optimized.

A photodetector converts the output optic signal, pre-amplified by an erbium-doped fiber amplifier (EDFA), into electric signal and the following spectrum analyzer extracts the high-frequency component $P(\omega)$ of interest. The EOC (r_{zzz}) of the poled Si_3N_4 can be derived from [5]:

$$P(\omega) = \eta \left[G \left(\frac{\partial P}{\partial \lambda} \right) \Big|_{\lambda=\lambda_0} \frac{\lambda_0 L}{2n_{\text{eff}} L_{\text{tot}}} n_{\text{SiN}}^3 r_{zzz} E_Z(\omega) \right]^2$$

where $\partial P/\partial \lambda$ is the slope of transmitted power spectrum of the device at λ_0 , n_{eff} is the effective index of the working mode of our device, n_{SiN} is the refractive index of Si_3N_4 , L_{tot} is the total length of the ring and L the length of where modulation field is applied, η is the power conversion efficiency of the photodetector, G is the gain of EDFA and $E_Z(\omega)$ is applied modulation field.

What we derive is the ZZZ component of EOC since the working mode is polarized in the same direction as the poling field as well as the modulation field.

We measure the r_{zzz} to be up to 26 fm/V in the device we engineered using this method, and we present non-decaying electro-optic modulation up to 15 GHz (Figure 2(b)). Compared to the pre-poling value, our engineering induces a > 50X enhancement at high frequency regime (> 4 GHz). Furthermore, we track the quantity of the induced r_{zzz} for 120 hours and no decay is observed.

Conclusions and Future Steps:

In conclusion, we demonstrate a permanent second order nonlinearity, up to 26 fm/V, built in silicon nitride available for modulation as fast as 15 GHz. We are working on fabrication of high-performance Si_3N_4 modulator based on this technique.

References:

- [1] E. Timurdogan, C. V. Poulton, M. J. Byrd, and M. R. Watts, "Electric field-induced second-order nonlinear optical effects in silicon waveguides," *Nature Photon* 11, 200-206 (2017).
- [2] A. Billat, D. Grassani, M. H. P. Pfeiffer, S. Kharitonov, T. J. Kippenberg, and C.-S. Brès, "Large second harmonic generation enhancement in Si_3N_4 waveguides by all-optically induced quasi-phase-matching," *Nat Commun* 8, 1016 (2017).
- [3] X. Lu, G. Moille, A. Rao, D. A. Westly, and K. Srinivasan, "Efficient photoinduced second-harmonic generation in silicon nitride photonics," *Nature Photonics* 1-6 (2020).
- [4] J. B. Khurgin, T. H. Stievater, M. W. Pruessner, and W. S. Rabinovich, "On the origin of the second-order nonlinearity in strained Si-SiN structures," *J. Opt. Soc. Am. B* 32, 2494 (2015).
- [5] M. Borghi, et al., "High-frequency electro-optic measurement of strained silicon racetrack resonators," *Opt. Lett.* 40, 5287 (2015).

Description of the Thermal Control using Metamaterials Project

CNF Project Number: 2527-17

Principal Investigator(s): Dr. David Crouse

User(s): Golsa Mirbagheri

Affiliation(s): Electrical and Computer Engineering Department, Clarkson University

Primary Source(s) of Research Funding: National Science Foundation (NSF)

Contact(s): dcrouse@clarkson.edu, gmirbagh@clarkson.edu

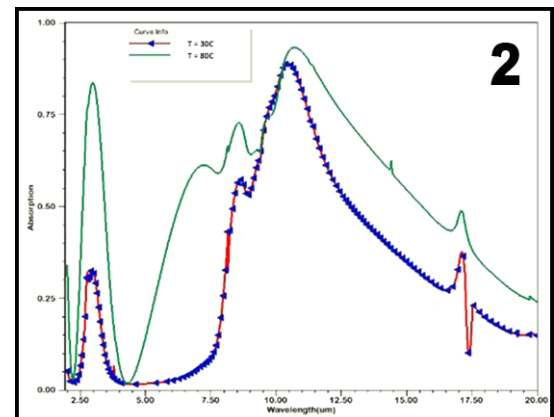
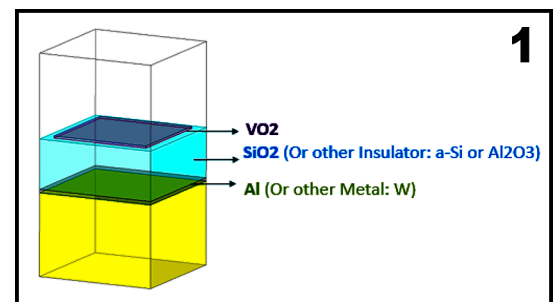
Primary CNF Tools Used: AJA sputter deposition, plasma enhanced chemical vapor deposition (PECVD)

Abstract:

In this project, we are going to fabricate a temperature-based metamaterial structure composed of vanadium oxide (VO_2) grating with the benefit of semiconductor to metal phase change. The thermochromic VO_2 is transparent, which acts as semiconductor in temperatures lower than critical temperature, but emits the light in higher temperature as a metal. The deposition of VO_2 film is under investigation by changing the oxygen and argon pressure along with applying temperature changes *in situ* in a sputtering chamber and also, by changing annealing methods.

Project Description:

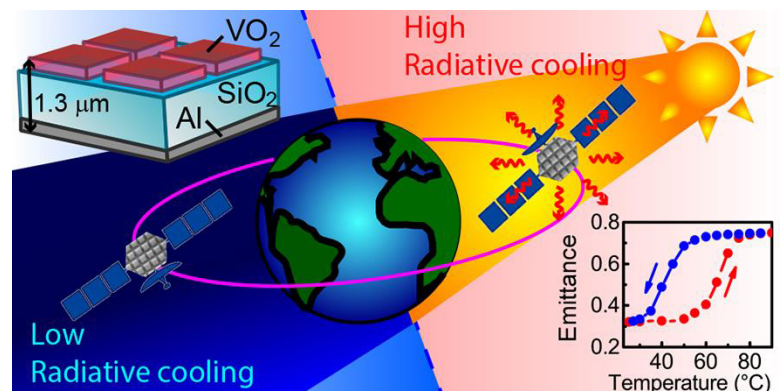
In this project we show the capabilities of metamaterials-based thermal controlling films. The metamaterial structure composed of VO_2 grating on top of SiO_2/Al substrate can retain heat when desired, while dissipate heat at other times, shown in Figure 1. VO_2 as a thermochromic material undergoes a semiconductor (monoclinic structure) to metal (rutile structure) transitions at a critical temperature of 68°C , accompanied by change in IR reflectivity and in resistivity, shown in Figure 2. The technology is unique such that it allows for passive thermal control of space-based instruments. We also developed a fabrication plan at the Cornell NanoScale Science and Technology Center (CNF) that allows for large-area fabrication of films, and designed the lithography mask for grating layer of the filter. If methods are developed to develop large-area films, then the technology can coat space-based instruments, as optical solar reflector (OSR), shown in Figure 3. The optical setup and reflector in addition to thermal control device is already accomplished to measure the reflection of filter at different temperatures in Clarkson University lab. Current thermal control systems require onboard electronics that add weight, size, complexity (i.e., SWaP-C).



References:

- [1] K. Sun, C. Riedel, A. Urbani, M. Simeoni, S. Mengali, M. Zalkovskij, B. Bilenberg, C. d. Groot and O. L. Muskens, "VO₂ Thermochromic Metamaterial-Based Smart Optical Solar Reflector," American Chemical Society Photonics, vol. 5, p. 2280-2286, 2018.

Figure 1, top: Metamaterial structure composed of VO_2 grating on top of insulator/metal substrate. Figure 2, middle: Absorption spectra of VO_2 increased in higher temp in comparison with lower temp. Figure 3, right: VO_2 based metamaterial structure as OSR shows the phase transition above and below 68°C critical temperature [1].



Metamaterial Spectrometer: A Low SWaP, Robust, High Performance Hyperspectral Sensor for Land and Atmospheric Remote Sensing

CNF Project Number: 2661-18

Principal Investigator & User: Lori Lepak

Affiliation(s): Phoebus Optoelectronics LLC

Primary Source(s) of Research Funding: National Aeronautics and Space Administration (NASA)

Contact(s): llepas@phoebusopto.com

Website: www.phoebusopto.com

Primary CNF Tools Used: ASML DUV stepper, Oxford 81 etcher, Logitech CMP, Zeiss Supra SEM

Abstract:

Since 2003, Phoebus Optoelectronics has enabled custom R&D solutions in the fields of Plasmonics, Metamaterials, Antennas, and Sensors. We work closely with our customers throughout device development, from simulation and design, to prototype realization, testing, and small volume manufacturing. Our R&D portfolio spans the spectral ranges of visible light, infrared, terahertz, and microwave radiation, for applications in high resolution imaging systems, wavelength and polarization filtering, tunable optical components, beam forming and steering, solar cells, renewable energy devices, and chemical and biological toxin sensors. We routinely partner with large, industry-leading businesses to develop products in all of these areas, jointly performing advanced testing and working together to scale up to medium- and large-volume manufacturing. Our agile team makes extensive use of the resources at the CNF for our nano/micro fabrication and testing, to provide cost efficiency and rapid turnaround. In the present report, we discuss the ongoing development of a metamaterial-based hyperspectral imaging filter.

Summary of Research:

Phoebus uses the resources of the CNF to fabricate plasmonic chips patterned with a metamaterial surface to enable Extraordinary Optical Transmission (EOT), a phenomenon unique to metastructures in which light is transmitted through apertures much smaller than the incident wavelength, at anomalously large intensities relative to the predictions of conventional aperture theory. EOT was first observed by T.W. Ebbesen in 1998 [1]. Since its founding in 2003, Phoebus has successfully harnessed EOT by incorporating metasurfaces into devices used to perform light filtering [2,3], photon sorting [4,5], polarimetric detection [6], high speed optical detection [7], and SPR plasmonic sensor chips [8].

In our current project, we are developing a hyperspectral imaging system, shown schematically in Figure 1. Our technology (Figure 1b) uses a metasurface to precisely target very narrow spectral bands of interest, enabling a significant reduction in the size and number of optical components relative to current state-of-the-art imaging systems (Figure 1a), which in turn will enable integration of our high-performance sensor onto weight-sensitive platforms (i.e., satellites) far more readily than existing systems. Our initial goal is to detect and image trace gases in the Earth's atmosphere in the midwave infrared (MWIR) region (defined as 3-5 μm wavelength), while reducing adjacent channel latency to less than 10 ms.

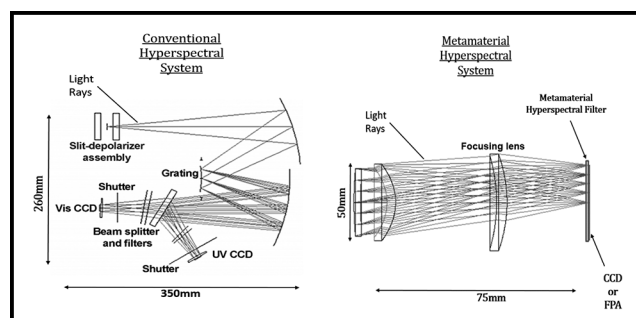


Figure 1: Phoebus's Metamaterial Spectrometer (MS) technology (right) eliminates much of the size and weight of conventional hyperspectral spectrometer technologies (left). Note the significant difference in scale of the two images.

Using the ASML DUV stepper, an entire wafer can rapidly be lithographically patterned with arrays of metastructures, as shown in Figure 2. In general, the optimal feature size and period of these metastructures depends primarily upon the desired wavelength of operation and the refractive indices of the constituent materials. In the MWIR, typical feature sizes are on the order of $\sim 1 \mu\text{m}$. As we can see in the optical microscope image in Figure 3, the ASML can easily produce highly uniform, large-area arrays of

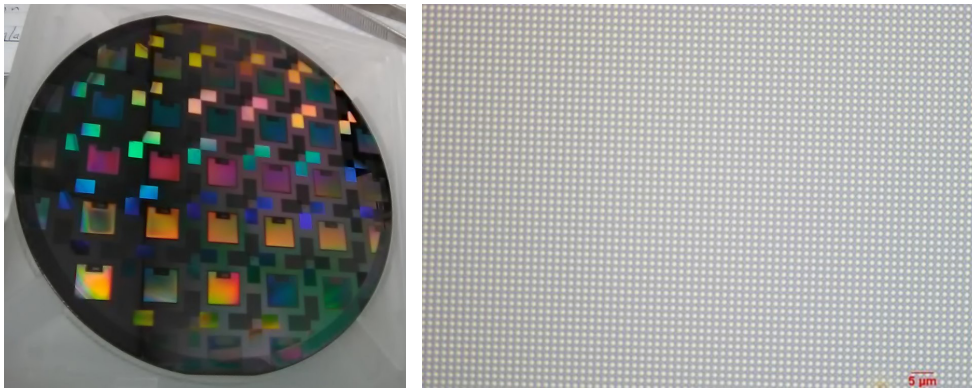


Figure 2, left: Wafer lithographically patterned with optical metastructures, using the ASML DUV stepper, Figure 3, right: Optical microscope image of test pattern of array of $\sim 1 \mu\text{m}$ pillars, also patterned on the ASML.

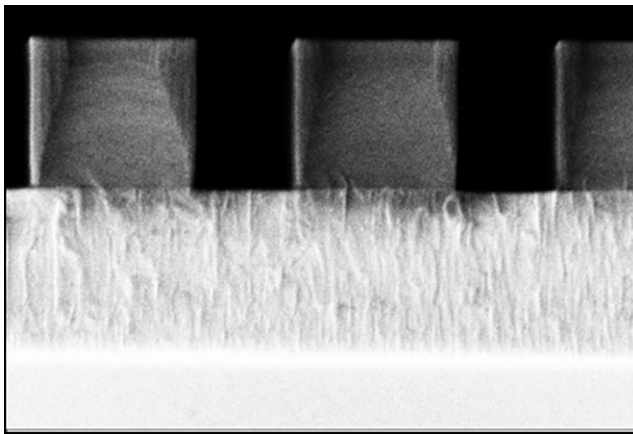


Figure 4: SEM image (cross section) of etched pillars with near-vertical sidewalls. Imaged at $\sim 90 \text{ kX}$ in the Zeiss Supra SEM, the grain structure of the etch stop layer is clearly visible.

test features of an appropriate size. Equally critical for photonics applications, relatively narrow spaces between these features can be etched with moderately high aspect ratios, to form structures with nearly vertical sidewalls, as shown in Figure 4. These vertical structures both minimize optical losses, and ensure that the real fabricated devices will perform as closely as possible to the optimal designs predicted by simulations.

Conclusions and Future Steps:

With strong, ongoing support from the National Aeronautics and Space Administration (NASA), we have successfully tested our first generation of MWIR devices. Having identified a few key areas for process improvements, we have begun fabrication of a second generation to fully optimize our MWIR device performance.

In addition, we have begun to adapt our overall metasurface technology to other spectral ranges, from the visible to the microwave, by substituting appropriate materials, and scaling feature sizes in proportion to the desired wavelength of imaging. We have just completed the fabrication of a visible/NIR-wavelength counterpart of the current technology, and are about to begin optical testing. The NIR/vis devices are fabricated using all of same tools as the MWIR project,

plus the Oxford PECVD and AJA sputter tool to deposit the thin films. Thus, the extensive resources of the CNF are enabling us to rapidly develop our Metamaterial Spectrometer technology for a broad range of imaging and sensing applications.

References:

- [1] Ebbesen, T.W., et al., "Extraordinary optical transmission through sub-wavelength hole arrays." *Nature*, (1998). 391(6668): p. 667-669.
- [2] Crouse, D. "Numerical modeling and electromagnetic resonant modes in complex grating structures and optoelectronic device applications." *Electron Devices, IEEE Transactions on* 52.11 (2005): 2365-2373.
- [3] Crouse, D., and Keshavareddy, P. "Polarization independent enhanced optical transmission in one-dimensional gratings and device applications." *Optics Express* 15.4 (2007): 1415-1427.
- [4] Lansey, E., Crouse, D., et al. "Light localization, photon sorting, and enhanced absorption in subwavelength cavity arrays." *Optics Express* 20.22 (2012): 24226-24236.
- [5] Jung, Y.U; Bendoyim, I.; Golovin, A.B.; and Crouse, D.T. "Dual-band photon sorting plasmonic MIM metamaterial sensor." *Proc. SPIE 9070, Infrared Technology and Applications XL, 90702X* (June 24, 2014); doi:10.1117/12.2050620.
- [6] Crouse, D., and Keshavareddy, P. "A method for designing electromagnetic resonance enhanced silicon-on-insulator metal-semiconductor-metal photodetectors." *Journal of Optics A: Pure and Applied Optics* 8.2 (2006): 175.
- [7] Mandel, I.; Gollub, J.; Bendoyim, I.; Crouse, D. Theory and Design of a Novel Integrated Polarimetric Sensor Utilizing a Light Sorting Metamaterial Grating. *Sensors Journal, IEEE*, (2012): Vol. PP, 99.
- [8] Lepak, L., et al. "Handheld chem/biosensor using extreme conformational changes in designed binding proteins to enhance surface plasmon resonance (SPR)" *Proc. SPIE 9862, Advanced Environmental, Chemical, and Biological Sensing Technologies XIII, 9862-7* (April 17, 2016); doi:10.1117/12.2222305.

Stoichiometric Silicon Nitride Growth for Nonlinear Nanophotonics

CNF Project Number: 2920-20

Principal Investigator & Remote User: Kartik Srinivasan

Affiliation(s): Joint Quantum Institute, NIST/University of Maryland, College Park, MD 20742, USA

Primary Source(s) of Research Funding: Defense Advanced Research Project Agency (DARPA),
National Institute of Standards and Technology (NIST)

Contact(s): kartiks@umd.edu

Website: <https://groups.jqi.umd.edu/srinivasan/>

Primary CNF Tools Used: Low pressure chemical vapor deposition (LPCVD) furnaces

Abstract:

Chip-integrated optical frequency combs based on integrated photonic resonators are an important technology for realizing precision measurement instrumentation, such as optical atomic clocks, in a compact and deployable format. The combs utilize nonlinear-wave mixing to spectrally redistribute a single-frequency pump laser into a spectrum of equally spaced parametric sidebands and have a behavior that depends on the interplay between dispersion, nonlinearity, dissipation, and gain. Dispersion depends on both the material chosen for the resonator and the geometry of the resonator. Stoichiometric silicon nitride grown via low-pressure chemical vapor deposition (LPCVD) has been a common choice for this application, but the precise growth conditions have varied in the literature. Here, we study the impact of varying growth conditions, all within the nominally stoichiometric growth regime, on dispersion and frequency comb generation.

Summary of Research:

We received several LPCVD-grown silicon nitride wafers from CNF, with the silicon nitride films grown on a $3\ \mu\text{m}$ thick SiO_2 layer, all on a Si substrate. The parameter varied between the different growth runs was the ratio of the precursor gases, which we stepped between 3:1 (ammonia:dichlorosilane) and 15:1 (ammonia:dichlorosilane).

The rest of the processing to create microring resonators was done at NIST, and the fabricated geometries were tested at UMD.

Figure 1 shows results of fits to spectroscopic ellipsometry data, revealing the wavelength-dependent refractive index behavior of the grown films. Although all films were grown within the typical precursor range claimed for stoichiometric films (e.g., ammonia:dichlorosilane $> 2:1$), there are clear differences between the films, both in terms of the range of refractive index values and the manner in which the refractive index varies (i.e., the dispersion). The impact of the precursor gas ratio on dispersion can be described by a quantity called the integrated dispersion, which in the context of microresonator frequency combs, describes the separation between cavity resonances and an equally spaced grid. This integrated dispersion, which we calculate using finite-element simulations that take the measured refractive index data into account, largely controls the frequency bandwidth of the comb, and is shown in Figure 2 (left side) for a fixed resonator geometry.

We see that both the maximum value of the integrated dispersion and the position of its zero crossings significantly differ as the gas ratio goes from 3:1 to 5:1 to 7:1.

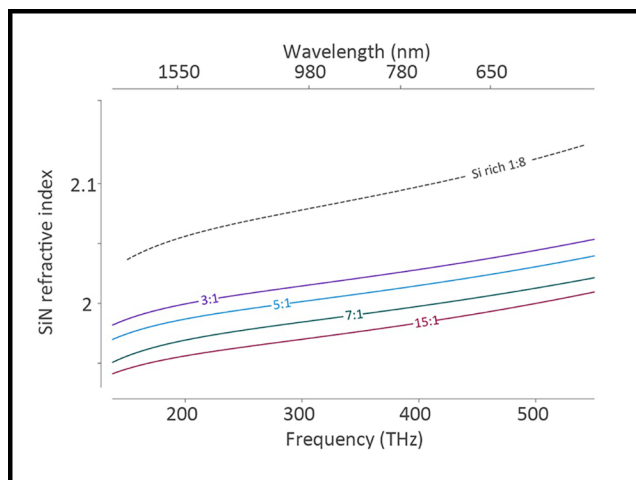


Figure 1: Wavelength/frequency-dependent refractive index values for silicon nitride films grown with varying ammonia:dichlorosilane ratios. 3:1, 5:1, 7:1, and 15:1 films are considered in this work. The refractive index of a Si-rich film (1:8 gas ratio) is shown for reference.

We then model the expected microcomb behavior using the Lugiato-Lefever Equation, which takes these integrated dispersion curves as an input. The predicted comb spectra in Figure 2 (right side) clearly show a significantly different comb bandwidth, with peaks at the extremities of the spectra, known as dispersive waves, having significantly different spectral positions and amplitudes.

To compensate for the shifts in the dispersive wave positions for differing growth gas ratios, we can tune the resonator geometry.

Figure 3 shows the results of measurements indicating such an effect, for resonators fabricated in 3:1 and 7:1 ammonia:dichlorosilane films. Here, the thickness of the two resonators differs by about 10 nm, but the high frequency dispersive waves are at nearly the same position (within 2 THz). In contrast, two resonators with a thickness differing by 10 nm, but fabricated in a fixed gas ratio film (e.g., 7:1), would be expected to show a > 15 THz shift.

Conclusions and Future Steps:

We have shown that the specific gas ratio within the nominally stoichiometric regime of LPCVD SiN growth has an impact on dispersion and microresonator frequency comb generation. Future work will utilize this ability to adjust material dispersion in combination with geometric dispersion engineering to create broadband microresonator combs to be used in compact optical atomic clocks.

References:

- [1] G. Moille, et al, CLEO, SF2A.4 (2021).

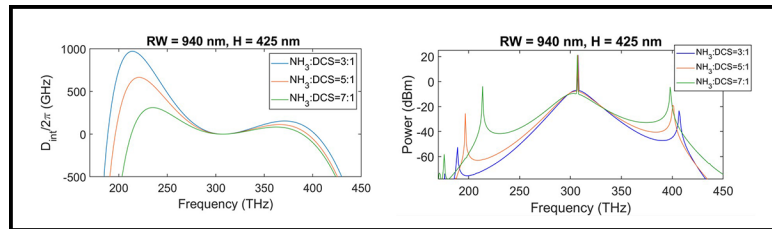


Figure 2: Simulation of the integrated dispersion (left) and expected soliton microcomb spectrum (right) for ring resonators with a fixed geometry and differing SiN films.

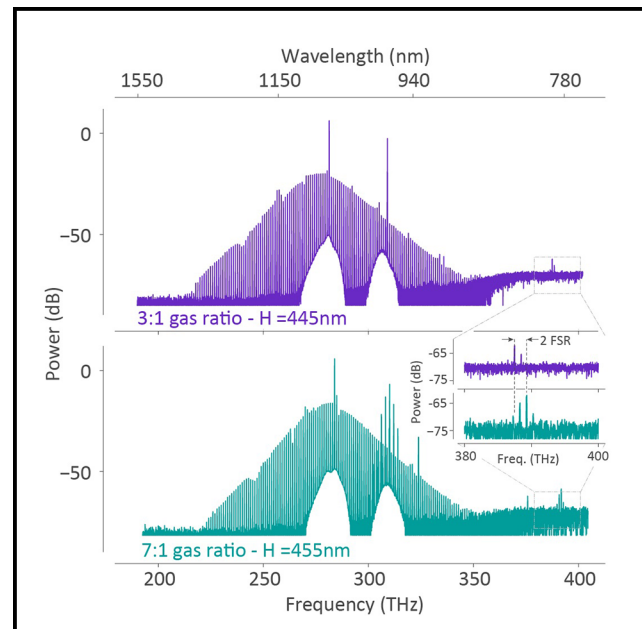


Figure 3: Measured soliton comb spectrum for two devices. The top (bottom) device is grown in a 3:1 (7:1) film, and the bottom device has a 10 nm greater film thickness.